Dynamic Article Links ▶

PAPER

Facile synthesis of a interleaved expanded graphite-embedded sulphur nanocomposite as cathode of Li–S batteries with excellent lithium storage performance

Yun-Xiao Wang,[ac] Ling Huang,*[a] Li-Chao Sun,[a] Su-Yuan Xie,[a] Gui-Liang Xu,[a] Shu-Ru Chen,[a] Yue-Feng Xu,[a] Jun-Tao Li,[b] Shu-Lei Chou,[c] Shi-Xue Dou[c] and Shi-Gang Sun*[a]

This paper reports the facile synthesis of a unique interleaved expanded graphite-embedded sulphur nanocomposite (S-EG) by melt-diffusion strategy. The SEM images of the S-EG materials indicate the nanocomposites consist of nanosheets with a layer-by-layer structure. Electrochemical tests reveal that the nanocomposite with a sulphur content of 60% (0.6S-EG) can deliver the highest discharge capacity of 1210.4 mAh g^{-1} at a charge–discharge rate of 280 mA g^{-1} in the first cycle, the discharge capacity of the 0.6S-EG remains as high as 957.9 mAh g^{-1} after 50 cycles of charge–discharge. Furthermore, at a much higher charge–discharge rate of 28 A g^{-1}, the 0.6S-EG cathode can still deliver a high reversible capacity of 337.5 mAh g^{-1}. The high sulphur utilization, excellent rate capability and reduced over-discharge phenomenon of the 0.6S-EG material are exclusively attributed to the particular microstructure and composition of the cathode.

Introduction

Rechargeable lithium-ion batteries (LIBs) are currently the predominant power sources for various portable electronic devices.[1] Nevertheless, the feasibility of using rechargeable lithium-ion batteries for pure electric vehicles (PEVs) and hybrid electric vehicles (HEVs) is restricted owing to the limited energy and power density, as well as the poor cycling lifespan of the LIBs. Substantial efforts to design and fabricate novel electrode materials for next-generation batteries with high-energy, high-power density, high-safety and low-cost have been therefore made in recent years.[2–8]

Sulphur possesses almost the highest theoretical capacity of 1675 mAh g^{-1} and the highest theoretical specific energy of 2600 Wh kg^{-1} among all known conventional cathode materials. Along with the abundant resources, low equivalent weight, low cost and environmental friendliness, sulphur has a significant potential to be used in next-generation batteries with high capacity and energy density. Despite the exceptional valuable characteristics of the Li–S battery, however, the sulphur cathode with an organic liquid electrolyte is facing challenges including low utilization of active material and severe capacity fading,

which are mainly ascribed to the insulating nature of sulphur and its final charge products, the solubility of the long chain poly-sulfide ions, and the deposition of insoluble Li_2S_2/Li_2S on the cathode.[9–15]

To successfully operate a Li–S battery, various strategies were developed, mainly in exploration of electrode coatings,[16] inorganic additives,[17] conductive additives and multifunctional binders,[18] as well as optimizing the organic electrolytes *etc.*[19,20] Nevertheless, the most effective method is to enable the sulphur to be well dispersed into a conductive and strong adsorbent additive. Different kinds of carbonaceous materials have received much attention because of their structure, conductivity and good electrochemical stability.[21–28] Remarkable progress has been made recently.[29,30] Among these studies, sulphur was loaded into ordered mesoporous carbon materials, which ensured a more efficient electronic contact and a high content of sulphur in the composite. As a consequence, a higher volumetric energy density, a higher capacity and a better rate capability have been achieved. Currently, a new kind of carbon material, graphene, has triggered extensive interest.[31,32] Graphene offers exceptional advantages owing to its high surface area, unique conductivity, ultrathin thickness, superior structural flexibility and good mechanical properties. More importantly, its nanostructures contain significant disorders, expansion of interlayer spacing and numerous active defects. The properties make it become a new anode material instead of commercial graphite,[33] a framework that can support active materials,[34–36] and a conductive additive in LIBs and supercapacitors.[37,38]

[a]State Key Laboratory of Physical Chemistry of Solid Surfaces, Department of Chemistry, College of Chemistry and Chemical Engineering, Xiamen, 361005, China. E-mail: huangl@xmu.edu.cn; sgsun@xmu.edu.cn; Fax: (+) 86-592-2180181; Tel: (+) 86-592-2180181
[b]School of Energy Research, Xiamen University, Xiamen, 361005, China
[c]Institute for Superconducting and Electronic Materials, University of Wollongong, NSW, 2522, Australia

In this paper, the expanded graphite (EG) consisted of graphene nanosheets, which was used as an efficient host and good electronic conductor of the sulphur cathode, and was synthesized by the modified Hummers' method.[39] The sulphur-expanded graphite(S-EG) nanocomposite was prepared by a simple melt-diffusion strategy. Superior lithium storage performances of the flexible interleaved S-EG nanocomposite have been revealed. The study has thrown light on the particular crucial role of the expanded graphite for maximum utilization of electrochemically active sulphur.

Experimental

Graphite oxide was prepared from natural graphite, which was cleaned using deionized water and dried in a vacuum oven. Graphene oxide (GO) was fabricated through a micro-area electric heating device at 1050 °C for 2 s to split apart the graphite oxide stacks weakly bound by van der Waals forces, then the expanded GO was reduced to EG using a mixed gas of H_2 and Ar at 450 °C for 5 h. The final S-EG products were prepared *via* a facile melt-diffusion strategy at 155 °C for 24 h at different fixed weight ratios of sulphur/carbon (20 : 80, 40 : 60, 60 : 40, 80 : 20) in a sealed Teflon container, which is denoted thereafter as 0.2S-EG, 0.4S-EG, 0.6S-EG, 0.8S-EG respectively.

Powder X-ray diffraction (XRD) (Philips X'Pert Pro Super X-ray diffractometer, Cu-Kα radiation), scanning electron microscopy (SEM) (HITACHI S-4800), transmission electron microscopy (TEM) (JEOL-2100, 200 Kv FEI Tecnai F30, 300 kV), nitrogen sorption isotherms (BET) (Micromeritics Tristar 3000), thermogravimetric analysis (TGA) (TG 209-F1), Raman spectroscopy (JOBINYvon HoribaRaman Spectrometer model HR800) and X-ray photoelectron spectroscopy (XPS) (Specs PHOIBOS 100 analyzer, Al kα) were applied to characterize the cathode materials. Raman spectra were collected by a 10 mW helium/neon laser at 632.8 nm excitation, which was filtered by a neutral density filter to reduce the laser intensity and a charge-coupled detector (CCD). XPS spectra were obtained exploiting Al Kα radiation and fixed analyser transmission mode. The pass energy was 60 eV for the survey spectra and 20 eV for particular elements.

The electrochemical measurements were carried out with 2025 coin cells assembled in an argon-filled glove box with lithium metal as anode. The cathode consisted of active materials (S-EG), conductivity agent (carbon black), and water-soluble binder (LA132) in a weight ratio of 7 : 2 : 1. The electrodes were separated by a separator material (Celgard 2400). The electrolyte is 1.0 M $LiN(CF_3SO_2)_2$ (LiTFSI) in a 1 : 1 v/v mixture of dimethoxyethane (DME) and 1,3-dioxolane (DOL).

Charge–discharge performances of the cells were tested with a constant current density of 280 mA g^{-1} at a cut-off potential of 1.5–3.0 V under room temperature by NEWARE BTS-610 instrument (Neware Technology Co., Ltd., Shenzhen, China). All the specific capacities are calculated based on the mass of sulphur. Cyclic voltammetry (CV) testing of the 0.6S-EG battery was performed on an electrochemistry working station CHI660 (Chenhua Co., Ltd., Shanghai, China) at the scan rate 0.05 mV s^{-1}. Electrochemical impedance spectroscopy (EIS) was conducted using a Biologic VMP-3 electrochemical workstation.

Results and discussion

The microstructure of the EG was characterized by SEM and TEM. As illustrated in Fig. 1a, the SEM image indicates that the EG possesses an ideal layer-by-layer structure. Fig. 1b illustrates that the EG consists of transparent sheets with some dark ripples. The transparency reveals that the sheets consist of graphene with only a few layers, and the dark ripples result from the scrolling and crumpling of nanosheets. Therefore, lots of nanovoids and nanocavities would exist in the scrolled graphene nanosheets which are favourable to anchor the active sulphur materials. The HRTEM image of stacked graphene layers is displayed in Fig. 1c. It is clearly visible that the (002) planes within all ripples are discontinuous and highly distorted, indicating that sp^2 domains are highly disordered. The pale areas between ripples are amorphous. These observations demonstrate that the graphene nanosheets are composed of highly distorted ripple-like sp^2 domains and amorphous carbon. The interlayer spacing of the (002) planes is 0.38 nm, which is larger than that of graphite (0.34 nm). The well-defined diffraction spots in the selected area electron diffraction pattern (SAED) (Fig. 1d) are fully indexed to the hexagonal graphite crystal structure, confirming the hexagonal graphite crystalline nature of the graphene nanosheets. The intensity difference of the diffraction pattern indicates that the graphene nanosheets consist of a multilayer structure.

The XRD patterns of pure EG, S-EG nanocomposites with different sulphur contents and a simple mechanical mixture of sulphur with EG are demonstrated in Fig. 2. The XRD profile of EG exhibits a broad weak (002) diffraction peak at 26°, which can be assigned to disordered stacks of graphene nanosheets. In comparison with the pattern of the S-EG mixture, the XRD spectra of the S-EG nanocomposite yields less peaks of smaller intensity, indicating that sulphur may be mainly anchored into the graphene framework and the excess sulphur becomes nano-sized crystalline sulphur in the cooling process. It is obvious that
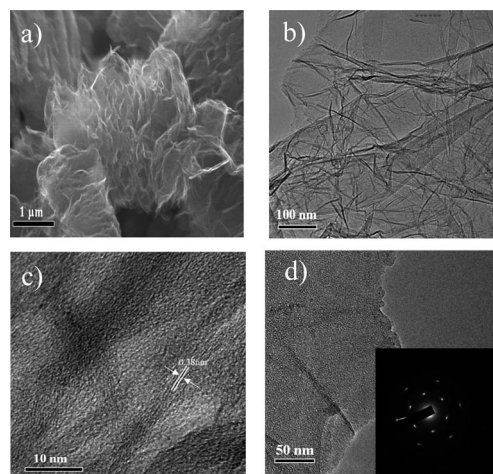

Fig. 1 (a) SEM image of the bulk graphene aggregate powders. (b) TEM image of stacked graphene nanosheets. (c) HRTEM image of stacked graphene nanosheets, where the lattice planes correspond to (002) planes with an interlayer distance of 0.38 nm. (d) HRTEM image of a section of a graphene nanosheet. The inset is the corresponding SAED pattern.
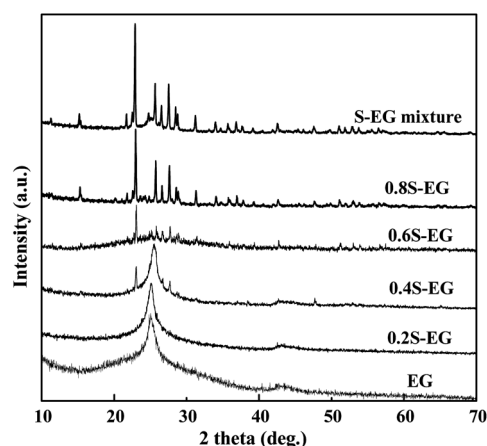
This journal is © The Royal Society of Chemistry 2012

J. Mater. Chem., 2012, **22**, 4744–4750 | 4745

Fig. 2 XRD profiles of expanded graphite (EG), 0.2S-EG, 0.4S-EG, 0.6S-EG and 0.8S-EG nanocomposites, and a mixture of sulphur with EG.

the amount of nanosized crystalline sulphur is enhanced with the increase in sulphur loading. As shown in Fig. 2, when the sulphur loading is 20%, there is only one broad diffraction peak which appears at approximately 26°. We couldn't observe any of the sulphur's diffraction peaks, which indicates that all of the sulphur exists in the graphene framework and no excess crystalline sulphur is formed. When the sulphur loading increases to 40% and 60%, small diffraction peaks can be observed in the XRD patterns of the S-EG nanocomposites, indicating the presence of the crystallized sulphur. When the sulphur loading increases to as high as 80%, the sharp diffraction peaks of sulphur can be detected, showing that sulphur is well crystallized. Since the state of sulphur in the graphene host affects the electrochemical performance of the nanocomposites, Raman and XPS are also used to further characterize the composites.

Raman spectra are extensively employed to characterize carbon materials, because the characteristic G-band ($\sim$1580 cm^{-1}) and D-band ($\sim$1350 cm^{-1}) are very sensitive to defects, disorders, edges and carbon grain size. A key structural parameter, the Raman intensity ratio of the D-band to G-band (I_D/I_G) can index the disorder degree and average size of the sp^2 domains. The G-band arises from the zone center E_{2g} mode, corresponding to ordered sp^2 bonded carbon, whereas the D-band is ascribed to edges, other defects and disordered carbon. The I_D/I_G ratio is therefore a measure of the degree of disorder and the average size of the sp^2 domains. As shown in Fig. 3a, the large I_D/I_G ratio (1.16) and wider G-band signify that the EG has a disordered, defective structure with small sp^2 domains, which is consistent with the SEM and TEM images. After adsorption/reaction of sulphur, the I_D/I_G ratio of all those samples declines to around 1.0. The phenomenon may be ascribed to the reaction of sulfur with oxygenated groups in the EG, including carboxyl groups at the edges, and epoxy, hydroxyl, and –C=C– groups in the basal plane. Therefore, sulphur loading can decrease the disorder degree of expanded graphite. In addition, the D-band position shifts, which relies on the degree and nature of the basal plane disorder and the excitation wavelength.[40]

In order to verify the reaction between the sulphur and the oxygenated groups from the EG, the sulphur state in the nanocomposites were characterized by XPS. Fig. 3b shows the XPS results of S (2p). The XPS spectra of S (2p) for the S-EG
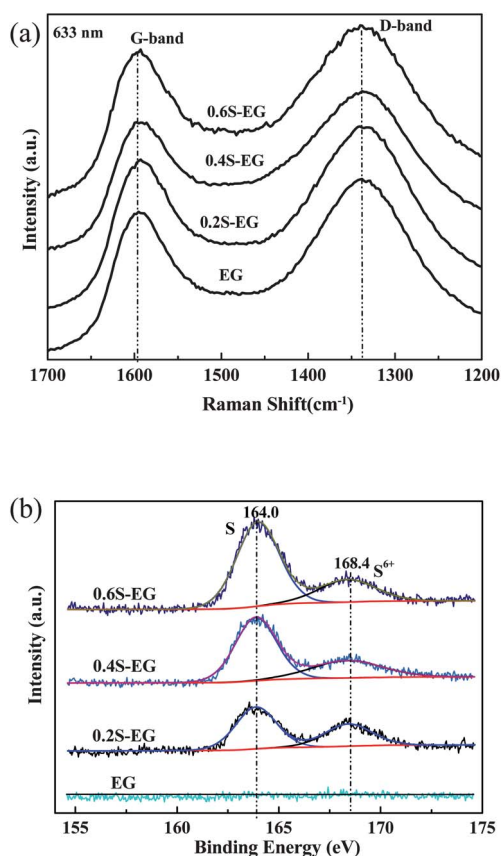

Fig. 3 (a) Raman spectra (G- and D-bands) and (b) XPS spectra of S (2p) for EG, 0.2S-EG, 0.4S-EG and 0.6S-EG nanocomposites.

composite have two peaks at 164.0 and 168.4 eV, corresponding to the state of S (S$_8$)[41] and S^{6+} (R–SO$_3$–R′ like in polystyrene sulfonate),[42] respectively. Since we didn't observe any S (2p) peaks for EG, the 2p (S^{6+}) peak is not from the H$_2$SO$_4$ which we used to prepare the graphite oxide. Although the sulphur composition from XPS is not accurate due to evaporation during measurements, the intensity of the peak in the XPS is still related to the composition of the materials. The intensities of the 2p (S$_8$) peaks increase as the sulphur contents increase, while the intensities of the 2p (S^{6+}) peaks increase as the graphene contents increase. This indicates that the S 2p (S^{6+}) peak is probably due to the reaction between sulphur and the oxygenated groups from the reduced graphene oxide. The large amount of reduced graphene contains more oxygenated groups. Therefore, we can get more S^{6+} in the 0.2S-EG sample.

The morphology of the 0.6S-EG nanocomposite was examined by SEM, TEM and elemental mappings. The morphology of 0.6S-EG nanocomposite shown by the SEM image in Fig. 4a is similar to that of pure EG, signifying that bulk crystalline sulphur completely disappears on the surface. Such a result implies that a large amount of sulphur existing as small nanoparticles is completely loaded into the interlayer spacing, edges and defects of the graphene nanosheets. The TEM image in Fig. 4b illustrates that no large bulk sulphur could be observed in the nanocomposite, which together with S elemental mapping verify the very small nanosize of sulphur particles (the sulphur nanoparticles have been marked with red arrows). The elemental
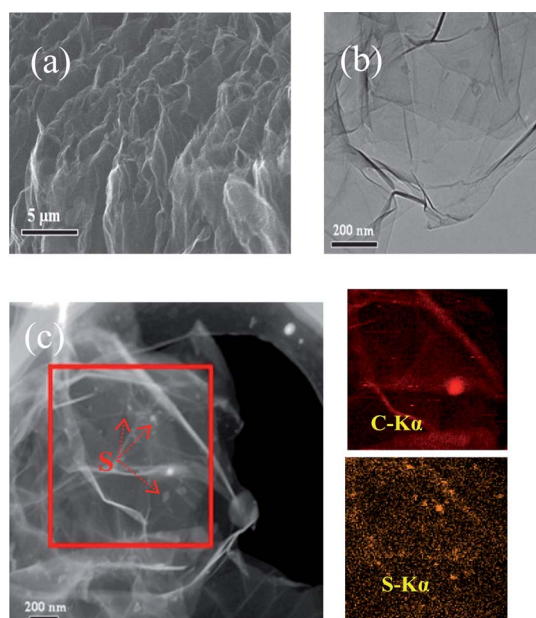
Fig. 4 (a) SEM image, (b) TEM image and (c) elemental mappings of carbon and sulphur corresponding to the area outlined by the red square in the dark field image of the 0.6S-EG nanocomposite.

mappings of sulphur and carbon of the area outlined by the red frame in Fig. 4c further corroborate that the sulphur is homogeneously embedded into the framework of the graphene host, which is ascribed to the favorable fluidity of molten sulphur.

The thermal decomposition characteristic of the materials under a nitrogen atmosphere was investigated by TGA. The TGA curves in Fig. 5a show that the 0.6S-EG nanocomposite almost ranges up to 60 wt% sulphur, which is consistent with the proportions of the added amount. It is evident that the sulphur embedded into EG is easier to sublime than the pure sulphur, which results in the sulphur nanoparticles being evenly anchored into the high surface of the EG framework. As shown in Fig. 5b, the pure graphene possesses a BET surface area of 289.11 m^2 g^{-1}, while the 0.6S-EG nanocomposite has a low BET surface area of 5.64 m^2 g^{-1}. Such a dramatic decrease in the BET surface area proves clearly the large loading of sulphur into the EG host after heating.

Electrochemical behavior of the S-EG cathode in a Li–S battery was investigated by galvanostatic charge–discharge measurement. Fig. 6a compares the cyclic performances of the S-EG cathodes with different sulphur contents. As for the 0.2S-EG cathode, the initial discharge capacity is 962.4 mAh g^{-1}, which is about 57.4% of the sulphur utilization based on the theoretical maximum 1675 mAh g^{-1}. The capacity increases with the increase in sulphur content in the nanocomposite. Upon increasing the sulphur content of the nanocomposite to 40% and then to 60%, the initial discharge capacity is respectively measured at 1020.7 mAh g^{-1} and 1210.4 mAh g^{-1}, corresponding to about 60.9% and 72.3% of sulphur utilization. However, when the sulphur content is increased further to 80%, the initial discharge capacity decreases to 854.1 mAh g^{-1} with 51.0% sulphur utilization. After 70 cycles, the 0.2S-EG cathode has a more obvious decay of capacity, dropping to 602.4 mAh g^{-1}. The 0.4S-EG and 0.6-EG cathodes show high capacity retention
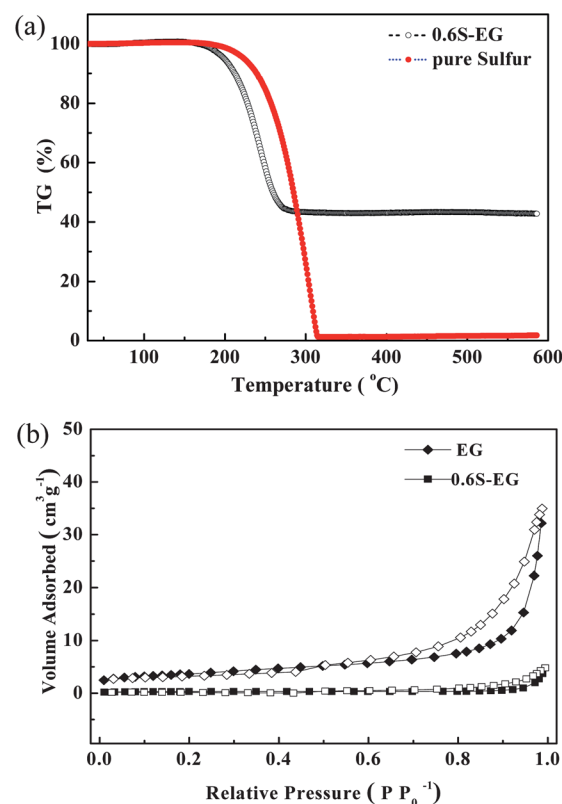

Fig. 5 (a) Thermogravimetric analysis (TGA) curves of pure sulphur and 0.6S-EG nanocomposite, (b) N$_2$ sorption isotherms of EG and 0.6S-EG nanocomposite.

during cell cycling, maintaining a discharge capacity of 728.0 mAh g^{-1} and 879.5 mAh g^{-1}, respectively. The 0.8S-EG cathode yields a very low discharge capacity of only 448.6 mAh g^{-1}. As shown in Fig. 6b, the 0.2S-EG electrode illustrates severe overdischarged phenomenon with the lowest initial Coulombic efficiency. The average Coulombic efficiency is about 110% for 0.6S-EG and 0.8S-EG. It is noticed that the 0.4S-EG shows a slight over-discharge phenomenon. The capacity retentions are shown in Fig. 6c. It can be found that the 0.6S-EG and 0.4S-EG have higher capacity retentions of 63.3% and 60.3% respectively, while the capacity retention is only 42.7% and 48.8% for 0.8S-EG and 0.2S-EG. Therefore, the sulphur content embedded into the EG can directly determine the overall performance of the nanocomposite. If the sulphur content is too low, the intrinsic polysulfides formed in the charge process are easier to dissolve in the organic electrolyte, leading to severe shuttle phenomenon. On the contrary, if the sulphur content is too high, more lowconductivity and insoluble Li$_2$S$_2$ or Li$_2$S can be produced in the discharge process, causing the capacity to fade rapidly. Therefore, only when the sulphur content is optimized can the nanocomposite cathode compensate both shortcomings to show excellent performance. Among the samples investigated, the 0.6S-EG cathode which had 60% sulphur content in the nanocomposite exhibited the best electrochemical performance with high capacity and retention rate.

To identify all the electrochemical reactions in the S-EG nanocomposite, the slow scan cyclic voltammogram of the 0.6S-EG cathode is demonstrated in Fig. 7a. Expanded
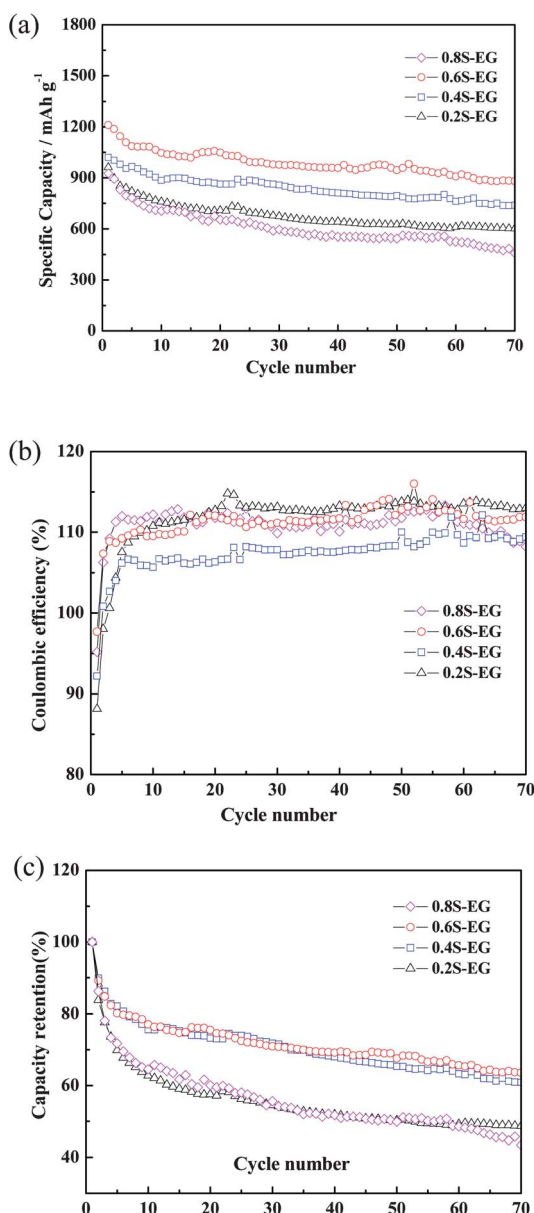
Fig. 6 The cyclic performance (a), Coulombic efficiency (the value of discharge capacity/charge capacity) (b), and capacity retention (c) of 0.2S-EG, 0.4S-EG, 0.6S-EG and 0.8S-EG nanocomposites.
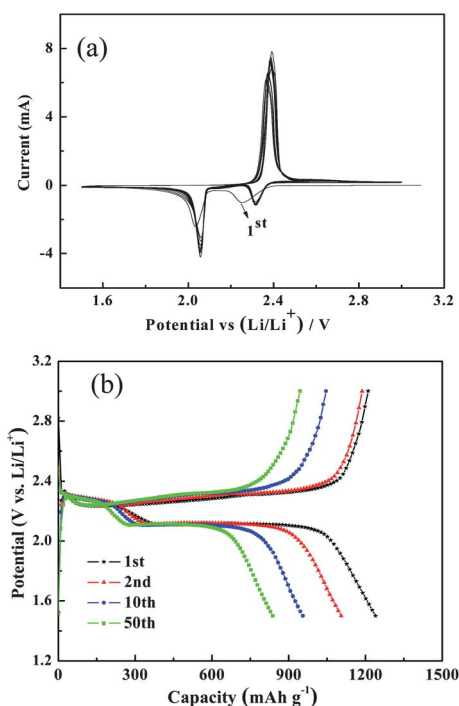

Fig. 7 (a) Cyclic voltammogram of the 0.6S-EG cathode in a coin cell at a scan rate of 0.05 mA s^{-1}. (b) Charge–discharge profiles of several cycles of the 0.6S-EG cathode at a current rate of 280 mA g^{-1}.

graphite in the nanocomposite is electrochemically inactive at this potential range. Two reduction peaks and one oxidation peak are observed, which result from the multistep reaction mechanisms of sulphur with lithium.[43–45] The first step is ascribed to the transformation of sulphur to lithium polysulfide (Li$_2$S$_n$, 2 < n < 8) at a high potential of about 2.3 V, the polysulfides readily dissolve in the electrolyte leading to the degradation of the Li–S battery system. The second step corresponds to the reduction of higher order lithium polysulfides to lithium sulfide (Li$_2$S$_2$, Li$_2$S) at a lower potential of about 2.1 V. One oxide peak at about 2.37 V is associated with the conversion to lithium polysulfide (Li$_2$S$_n$, n > 2), implying that all the polysulfides are transformed into intermediate S$_8^{2-}$ with the most facile oxidation kinetics.[46] During the subsequent

cycles, both cathodic and anodic peaks are positively shifted, which is ascribed to polarization of the electrode materials in the first cycle. This electrode shows very stable repeatability in the subsequent 10 cycles, signifying that the nanocomposite cathode has a high reversible capacity and long cycling lifespan. Fig. 7b displays the charge–discharge curves of the 0.6S-EG nanocomposite. Two typical plateaus for the S-electrode at respectively 2.3 V and 2.1 V are observed in the discharge process, which can be assigned to the two-step reaction of sulphur with lithium in the discharge process, only one plateau is observed in the charge process at about 2.37 V. The positions of the plateaus correspond well to the typical peaks of the S-electrode in the CV curves. After 50 cycles, the plateau is still evident and stable, demonstrating the excellent cyclic performance of the nanocomposite cathode. The electrochemical properties of the 0.6S-EG nanocomposite electrode in terms of capacity and over-discharged phenomenon are much better in comparison with results reported recently.[47,48]

Moreover, an excellent rate capability and lower over-discharged phenomenon are also achieved. As shown in Fig. 8, the discharge capacity is 1220 mAh g^{-1} at 280 mA g^{-1}, i.e. 72.8% of its theoretical capacity. With the rapid increase in the charge–discharge current density, the capacity decreases slowly and the over-discharged phenomenon dramatically dwindles. It can be seen that even at the highest current density of 28 A g^{-1}, which corresponds to a time of 35 s to fully discharge the total capacity, the measured discharge capacity is still as high as 337.5 mAh g^{-1}, which is 20.2% of its theoretical capacity. When the current density directly returns to the initial value (280 mA g^{-1}) after 25 cycles, the nanocomposite electrode recovers its original capacity.
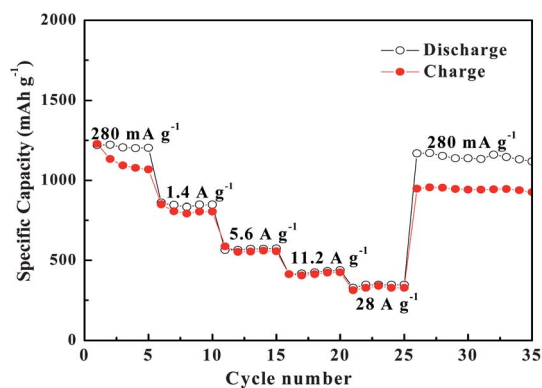
Fig. 8 Rate capability of the 0.6S-EG nanocomposite cathode at different current rates.

Fig. 9 shows the comparison of the electrochemical impedance spectra (EIS) between 0.6S-CB (using carbon black instead of all expanded graphite in the electrode) and 0.6S-EG, the Nyquist plots were measured at a discharged potential of 1.95 V *vs.* Li/Li$^+$ after charge–discharge for five cycles. The data were collected from 1 MHz to 10 mHz. The combination resistance (R_Ω) is determined by the ionic resistance of the electrolyte, the intrinsic resistance of the active materials and the contact resistance at the active material/current collector interface, corresponding to the intercept at the real axis Z'.[49] The charge transfer resistance (R_{ct}) represents the kinetic resistance of the charge transfer at the electrode–electrolyte boundary or intrinsic charge transfer resistance of the porous electrodes, corresponding to the semi-circle in the medium-frequency region. The Warburg impedance (W) is associated with Li-ion diffusion in the electrode, corresponding to the inclined line at low frequency. The equivalent circuit model was shown to analyze the impedance spectra in the inset of Fig. 9. As shown in the Nyquist plots, the electrodes have similar Li-ion diffusion rates. The R_{ct} value is calculated to be 150 Ω for 0.6S-EG, which is lower than 155.3 Ω for 0.6S-CB, indicating that S-EG has a higher electronic and ionic conductivity than 0.6S-CB. Remarkably, the combination resistance of 0.6S-EG (16.4 Ω) is much lower than 0.6S-CB (99.5 Ω), which demonstrated that the EG dramatically decreased the intrinsic resistance of the sulphur electrode. The EIS results also explain
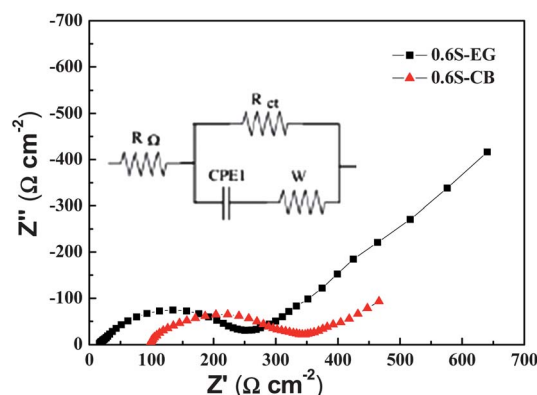
why the 0.6S-EG has the excellent cycling stability and rate properties.

The unique excellent performances of the 0.6S-EG cathode are mainly attributed to the multifunctional expanded graphite composed of graphene nanosheets: (i) the high surface area and ultra thinness of graphene nanosheets are helpful for accessibility of the electrolyte and rapid diffusion of lithium ions ingress/egress to react with the sulphur; (ii) the interlayer spacing/edges/defects within the EG framework as good containers of sulphur can confine sulphur and polysulfides in the framework, which are favourable to improve the electronic conductivity of sulphur and abate the dissolution of the polysulfides in the liquid electrolyte. As a consequence the cycle life and the reversible capacity of the electrode have both been extended; (iii) graphene layers can act as mini-current collectors which facilitate the fast transportation of electrons during the charge–discharge process, resulting in the excellent rate behavior of the electrode. As demonstrated in this paper, the sulphur content also plays a great role in improving the performance of the S-EG cathode.

Conclusions

In the current paper, the well-designed and high-powered S-EG nanocomposite has been synthesized by a straightforward and fast melt-diffusion strategy. The sulphur content in the nano-composites was varied from 20% to 80%. It has been demon-strated that the cathode of the nanocomposite with 60% sulphur content exhibits the highest capacity. Its initial discharge capacity is 1210.4 mAh g^{-1} at a charge–discharge rate of 280 mA g^{-1}, and retains as high as 879.5 mAh g^{-1} after 70 cycles. Moreover, an improved cyclic ability, a dwindled overdischarged phenomenon and an outstanding rate capability are also confirmed. The unique excellent performances of the 0.6S-EG nanocomposite cathode are mainly attributed to the multifunc-tional expanded graphite and the particular microstructure of the nanocomposite. Such flexible expanded graphite-embedded sulphur cathode is a promising candidate for the next-generation rechargeable batteries for important applications such as electric vehicles.

Acknowledgements

References

1 P. G. Bruce, *Solid State Ionics*, 2008, **179**, 752.
2 B. Kang and G. Ceder, *Nature*, 2009, **458**, 190.
3 Y. K. Sun, S. T. Myung, B. C. Park, J. Prakash, I. Belharouak and K. Amine, *Nat. Mater.*, 2009, **8**, 320.
4 Y. G. Wang, Y. R. Wang, E. J. Hosono, K. X. Wang and H. S. Zhou, *Angew. Chem., Int. Ed.*, 2008, **47**, 7461.
5 F. Jiao, J. L. Bao, A. H. Hill and P. G. Bruce, *Angew. Chem., Int. Ed.*, 2008, **47**, 9711.
6 E. Hosono, T. Kudo, I. Honma, H. Matsuda and H. S. Zhou, *Nano Lett.*, 2009, **9**, 1045.

Fig. 9 Nyquist plots of 0.6S-CB (a) and 0.6S-EG (b) at an open circuit potential of 2.1 V.

7 K. T. Nam, D. W. Kim, P. J. Yoo, C. Y. Chiang, N. Meethong, P. T. Hammond, Y. M. Chiang and A. M. Belcher, *Science*, 2006, **312**, 885.
8 D. Marmorstein, T. H. Yu, K. A. Striebel, F. R. McLarnon, J. Hou and E. J. Cairns, *J. Power Sources*, 2000, **89**, 219.
9 R. D. Rauh, F. S. Shuker, J. M. Marston, S. B. Brummer and J. Inorg, *J. Inorg. Nucl. Chem.*, 1977, **39**, 1761.
10 S. E. Cheon, K. S. Ko, J. H. Cho, S. W. Kim, E. Y. Chinand and H. T. Kim, *J. Electrochem. Soc.*, 2003, **150**, A800.
11 B. H. Jeon, J. H. Yeon, K. M. Kim and I. J. Chung, *J. Power Sources*, 2002, **109**, 89.
12 R. D. Rauh, K. M. Abraham, G. F. Pearson, J. K. Surprenant and S. B. Brummer, *J. Electrochem. Soc.*, 1979, **126**, 523.
13 H. Yamin, A. Gorenshtein, J. Penciner, Y. Sternberg and E. Peled, *J. Electrochem. Soc.*, 1988, **135**, 1045.
14 J. Shim, K. A. Striebel and E. J. Cairns, *J. Electrochem. Soc.*, 2002, **149**, A1321.
15 S. E. Cheon, K. S. Ko, J. H. Cho, S. W. Kim, E. Y. Chin and H. T. Kim, *J. Electrochem. Soc.*, 2003, **150**, A796.
16 J. H. Lee, H. Y. Lee, S. M. Oh, S. J. Lee and S. M. Lee, *J. Power Sources*, 2007, **166**, 250.
17 A. Gorkovenko, U.S. Patent, 2001, 210, p. 831 B1.
18 J. H. Shin, K. W. Kim and H. J. Ahn, *Mater. Sci. Eng., B*, 2002, **95**, 148.
19 W. K. Wang, Y. Wang, Y. Q. Huang, C. J. Huang, Z. B. Yu, H. Zhang, A. B. Wang and K. G. Yuan, *J. Appl. Electrochem.*, 2010, **40**, 321.
20 D. Aurbach, E. Pollak, R. Elazari, G. Salitra, C. S. Kelley and J. Affinito, *J. Electrochem. Soc.*, 2009, **156**, A694.
21 J. Wang, L. Z. Ling, J. Yang, C. Wan and C. Jiang, *Electrochim. Acta*, 2003, **48**, 1861.
22 B. Zhang, C. Lai, Z. Zhou and X. P. EGo, *Electrochim. Acta*, 2009, **54**, 3708.
23 S. C. Han, M. S. Song, H. Lee, H. S. Kim, H. J. Ahn and J. Y. Lee, *J. Electrochem. Soc.*, 2003, **150**, A889.
24 J. Wang, S. Y. Chew, Z. W. Zhao, S. Ashraf, D. Wexler, J. Chen, S. H. Ng, S. L. Chou and H. K. Liu, *Carbon*, 2008, **46**, 229.
25 C. D. Liang, N. J. Dudney and J. Y. Howe, *Chem. Mater.*, 2009, **21**, 4724.
26 X. L. Ji, K. T. Lee and L. F. Nazar, *Nat. Mater.*, 2009, **8**, 500.
27 Y. L. Cao, X. L. Li, I. A. Aksay, J. Lemmon, Z. Nie, Z. G. Yang and J. Liu, *Phys. Chem. Chem. Phys.*, 2011, **13**, 7660.
28 J. Z. Wang, L. Lu, M. Choucair, J. A. Stride, X. Xu and H. K. Liu, *J. Power Sources*, 2011, **196**, 7030.
29 W. Wei, J. L. Wang, L. J. Zhou, J. Yang, B. Schumann and Y. N. Li, *Electrochem. Commun.*, 2011, **13**, 399.
30 S. R. Chen, Y. P. Zhai, G. L. Xu, Y. X. Jiang, D. Y. Zhao, J. T. Li, L. Huang and S. G. Sun, *Electrochim. Acta*, 2011, **56**, 9549.
31 A. K. Geim and K. S. Novoselov, *Nat. Mater.*, 2007, **6**, 183.
32 A. K. Geim, *Nature*, 2009, **324**, 1530.
33 P. C. Lian, X. F. Zhu, S. Z. Liang, L. Zhong, W. S. Yang and H. H. Wang, *Electrochim. Acta*, 2010, **55**, 3909.
34 Z. S. Wu, W. C. Ren, L. Wen, L. B. EGo, J. P. Zhao, Z. P. Chen, G. M. Zhou, F. Li and H. M. Cheng, *ACS Nano*, 2010, **4**, 3187.
35 P. C. Lian, X. F. Zhu, H. F. Xiang, Z. Li, W. S. Yang and H. H. Wang, *Electrochim. Acta*, 2011, **56**, 834.
36 B. Zhang, Q. B. Zheng, Z. D. Huang, S. W. Oh and J. K. Kim, *Carbon*, 2011, **49**, 4524.
37 F. Y. Su, C. H. You, Y. B. He, W. Lv, W. Cui and F. M. Jin, *J. Mater. Chem.*, 2010, **20**, 9644.
38 G. H. Yu, L. B. Hu, N. Liu, H. L. Wang, M. Vosgueritchian, Y. Yang, Y. Cui and Z. N. Bao, *Nano Lett.*, 2011, **11**, 4438.
39 W. Hummers and R. Offeman, *J. Am. Chem. Soc.*, 1958, **80**, 1339.
40 A. Gupta, G. Chen, P. Joshi, S. Tadigadapa and P. C. Eklund, *Nano Lett.*, 2006, **6**, 2667.
41 C. D. Wangner, W. M. Riggs, L. E. Davis, J. F. Moulder, G. E. Muilenberg, *Handbook of X-ray photoelectron spectroscopy*, Perkin-Elmer Corporation, 2919.
42 E. Vitoratos, S. Sakkopoulos, E. Dalas, N. Paliatsas, D. Karageorgopoulos, F. Petraki, S. Kennou and S. A. Choulis, *Org. Electron.*, 2009, **10**, 61.
43 E. Peled, Y. Sternberg, A. Gorenshtein and Y. Lavi, *J. Electrochem. Soc.*, 1989, **136**, 1621.
44 H. Yamin, A. Gorenshtein, J. Penciner, Y. Sterberg and E. Peled, *J. Electrochem. Soc.*, 1988, **135**, 1045.
45 M. M. Sun, S. C. Zhang, T. Jiang, L. Zhang and J. H. Yu, *Electrochem. Commun.*, 2008, **10**, 1819.
46 H. Yamin, J. Penciner, A. Gorenshtain, M. Elam and E. Peled, *J. Power Sources*, 1985, **14**, 129.
47 H. L. Wang, Y. Yang, Y. Y. Liang, J. T. Robinson, Y. G. Li, A. Jackson, C. Yi and H. J. Dai, *Nano Lett.*, 2011, **11**, 2644.
48 R. Elazari, G. Salitra, A. Garsuch, A. Panchenko and D. Aurbach, *Adv. Mater.*, 2011, **23**, 5641.
49 J. Gamby, P. L. Taberna, P. Simon, J. F. Fauvarque and M. Chesbeau, *J. Power Sources*, 2001, **101**, 109.